Treatment of AlSi12 feedstock with water to manufacture multi-material parts by laser powder bed fusion process: A potential route for the fabrication of inorganic 3D metamaterials

F Lanoue, F Veron, I Pasquet, K Kiryukhina, V Baco-Carles, O Vendier, Ph Tailhades

Journal of Materials Research and Technology 27 (2023) 4772–4786

Contents lists available at ScienceDirect

Journal of Materials Research and Technology

journal homepage: www.elsevier.com/locate/jmrt

Treatment of AlSi12 feedstock with water to manufacture multi-material parts by laser powder bed fusion process: A potential route for the fabrication of inorganic 3D metamaterials

F. Lanoue [a,b], F. Veron [c], I. Pasquet [b], K. Kiryukhina [a], V. Baco-Carles [b], O. Vendier [c], Ph Tailhades [b,*]

[a] Centre National d'Etudes Spatiales CNES, 18 Avenue Edouard Belin, 31 400, Toulouse, France
[b] Institut Carnot Chimie Balard Cirimat, Cirimat UMR CNRS 5085, Université Toulouse 3 Paul Sabatier, 118 Route de Narbonne, 31 062, Toulouse, Cedex 9, France
[c] Thales Alenia Space, 26 Avenue Jean François Champollion, 31 100, Toulouse, France

ARTICLE INFO

Handling Editor: SN Monteiro

Keywords:
Metamaterials
3D multi-materials
Aluminum-alumina assemblies
Laser powder bed fusion
Aluminum-water reaction
Hydrogen generation

ABSTRACT

A new L-PBF process is proposed to manufacture, from a single powder chemically activated by pure hot water, parts comprising in selected areas of space, a ceramic or a metal alloy. The chemical activation of the starting alloy powder, the melting and densification of the metallic zones as well as the oxidation of metal alloy powder and sintering of the ceramic zones, have been studied and optimized. The results obtained allowed the realization of multi-material functional structures. Thus, small coaxial conductors have been fabricated. Beyond these relatively simple parts, 2D and 3D periodic structures made of ceramics and metal have been successfully realized. The achievement of these periodic structures gives hope for the further development of 3D inorganic metamaterials for microwave applications.

1. Introduction

Laser-Powder Bed Fusion (L-PBF) is an additive manufacturing process that has already attracted interest from the aerospace, automotive, medical and jewelry industries [1] and continues to grow. Conventional L-PBF machines however, have only one powder supply tank. As a consequence in their basic version they cannot produce parts in which the spatial distribution of several materials can be controlled [2]. At best, it is possible to produce composites that randomly combine several materials at the micro- or nanoscale [3–5]. This is a major drawback that limits the use of the conventional L-PBF process [6]. To overcome this difficult technological constraint [7] and to be able to build parts in which discrete or gradual changes of materials are found [8], special machines have been designed. They can be classified into the following four categories [9].

The blade-based dissimilar powder spreading technique [10] deposits two materials each contained in a feed compartment. These dissimilar materials can only be layered but cannot be arranged in the same plane. This process only produces multilayer structures along the vertical axis, which also results in rough interfaces between the two materials.

The ultrasonic-based dissimilar powder spreading method uses two silos containing different powders. The latter allows for local and programmed spreading of controlled quantities of one or other powder, thanks to an ultrasonic device. This process leads to the production of 3D multi-material parts [11]. However, the slowness of the manufacturing process remains a weak point.

A third technology, called electrophotographic spreading of dissimilar powder, is inspired by the principle of desktop laser printers. It allows to deposit locally, in thin layers, particles from different toners [12]. The laser fusion makes it possible to combine different materials in the same plane and to manufacture parts composed of at least two materials distributed in the three directions of space. Spreading systems based on a similar principle, in which the powders are supported on the surface of a drum by purely mechanical forces, are adaptable to various L-PBF or binder jetting machines [13]. They are currently marketed by Aerosint [14] and offer the possibility of building multi-material parts in three dimensions, without generating a significant mixing of the powders used.

Finally, the fourth variant of these multi-material processes is the

* Corresponding author.
E-mail address: philippe.tailhades@univ-tlse3.fr (P. Tailhades).

https://doi.org/10.1016/j.jmrt.2023.10.254
Received 3 May 2023; Received in revised form 3 October 2023; Accepted 24 October 2023
Available online 7 November 2023

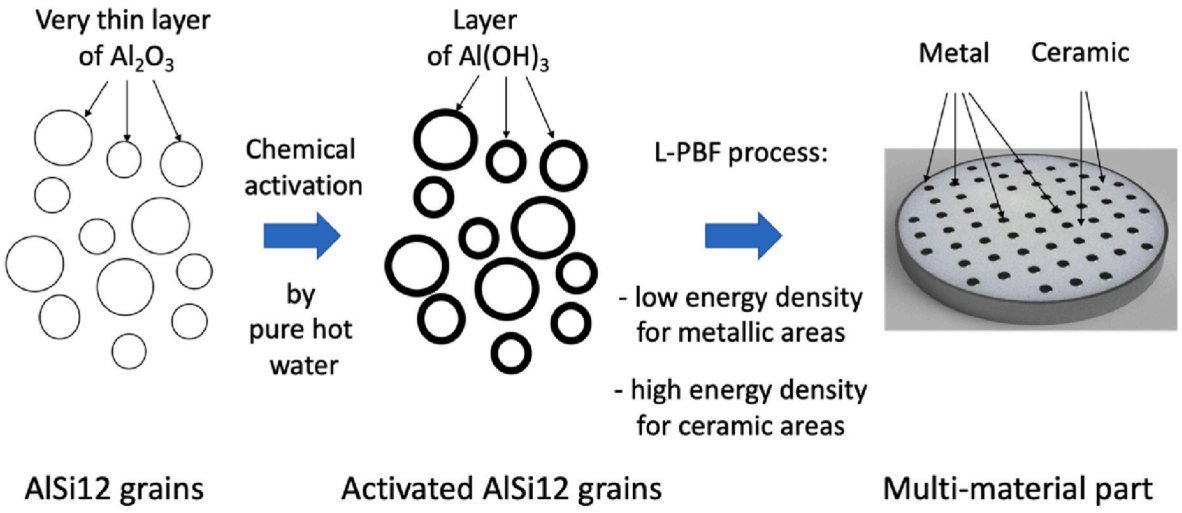

Fig. 1. Diagram of the manufacturing process for metal ceramic parts.

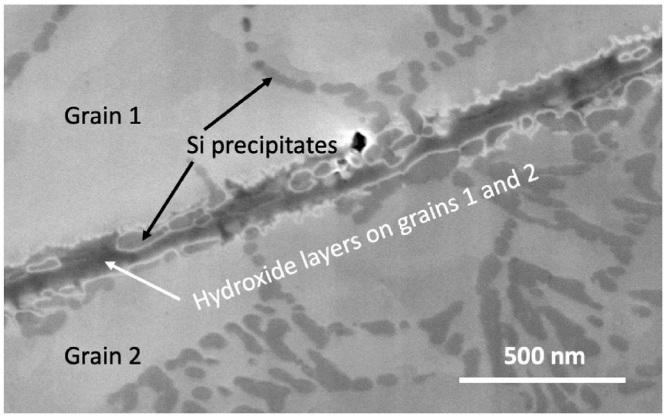

Fig. 2. View of a FIB cross-section of two compacted grains from a powder activated at 80 °C for 3 min 30 s. Silicon precipitates, which appear dark grey in the aluminum grains and in hydroxide layers, have not been attacked by hot water.

'Blade + ultrasound' hybrid method for spreading dissimilar powders. In this case, a blade spreads the powder making up the main volume of the part, which is then fused by the laser. A portion of the untreated powder is removed by a micro-suction system and replaced by a second powder supplied by ultrasonic pipettes. The latter is in turn fused by the laser to form the second material of the part under construction [15]. The recycling of the residual powders is difficult due to their mixing, but this process allows the use of several pipettes and the construction of parts with more than two different materials.

Very recently, colloid nebulization has also been proposed to fabricate multi-materials by L-PBF process [16]. Small quantities of tungsten carbide can be added to 316-L alloy by this method. However, with the exception of the recently introduced Aerosint devices, which transform the L-PBF process into a true Multi-Material Additive Manufacturing (MMAM) technique, machines operating on the concepts described briefly above, are not commercially available at this time.

The most studied materials for L-PBF process are iron alloys, but aluminum alloys are also receiving much attention, especially those containing silicon and/or magnesium [17–19]. For L-PBF, the controlled combination in three dimensions of space, of aluminum or its alloys with another metallic or ceramic material, obviously poses similar problems to those mentioned above. Indeed, the bibliography only reports work on ceramic-reinforced aluminum composites [20] or iron/iron-aluminum alloy multilayers [21]. However, a new approach has recently been proposed [22]. It consists in chemically activating an aluminum alloy powder with an alkaline base, to give it a higher reactivity to oxygen. Thus, from this single powder, a conventional machine operating in air or an oxygen-enriched atmosphere, can either fuse at low energy density, zones in the metallic state, or oxidize and sinter other zones in ceramic form, by simply applying a higher laser energy density to them. Metal and ceramic can thus be combined in all three directions of space.

Aluminum reacts with pure water by releasing heat and hydrogen [23,24]. This exothermic reaction can be easily achieved at room temperature with nano-sized aluminum powders [25]. Aluminum is therefore potentially a material for large-scale energy storage [26] or for small mobile devices [27], as the hydrogen generated upon contact with water can be converted into electricity by fuel cells. But beyond these potential technological applications, the reaction of water with aluminum could be used to activate AlSi12 alloy powders, implemented in the multi-material L-PBF process proposed by Veron et al. [22]. The main advantage of chemical activation with pure water would be absence of sodium or potassium pollution from the alkaline base, used to etch the starting metal powder. The ease of recycling liquid effluents, almost exclusively made up of water, as well as the potential valorization of the hydrogen gas produced, would also be significant advantages of this original mode of activation. However, the powders intended for a L-PBF process, made of an aluminum alloy on the one hand, and grains of a few tens of micrometers on the other hand, differ strongly from the pure nanometric aluminum most often used for energy devices. The activation of micrometric powders by water therefore requires specific experimental conditions, which remain to be developed. In particular, the activation must be controlled so as not to degrade the total volume of the grains and to affect only their surface.

As multi-material additive manufacturing by L-PBF is a major issue, it is interesting to evolve the process proposed by Veron et al. considering its virtues related to the use of a single powder and the use of conventional L-PBF machines. The first objective of the present work was therefore to search for suitable processing conditions allowing the activation of micrometric AlSi12 powders, by a simple reaction with water. It was thus necessary to find activation conditions allowing the oxidation of the powders and their sintering in the form of ceramics, under the effect of a high energy density brought by the laser of the L-PBF machines. But it was also necessary that these powders could be melted for lower laser energy densities, in order to form mechanically resistant metallic zones.

This work also has a second objective. It is to demonstrate that from a single activated powder and by implementing a conventional L-PBF

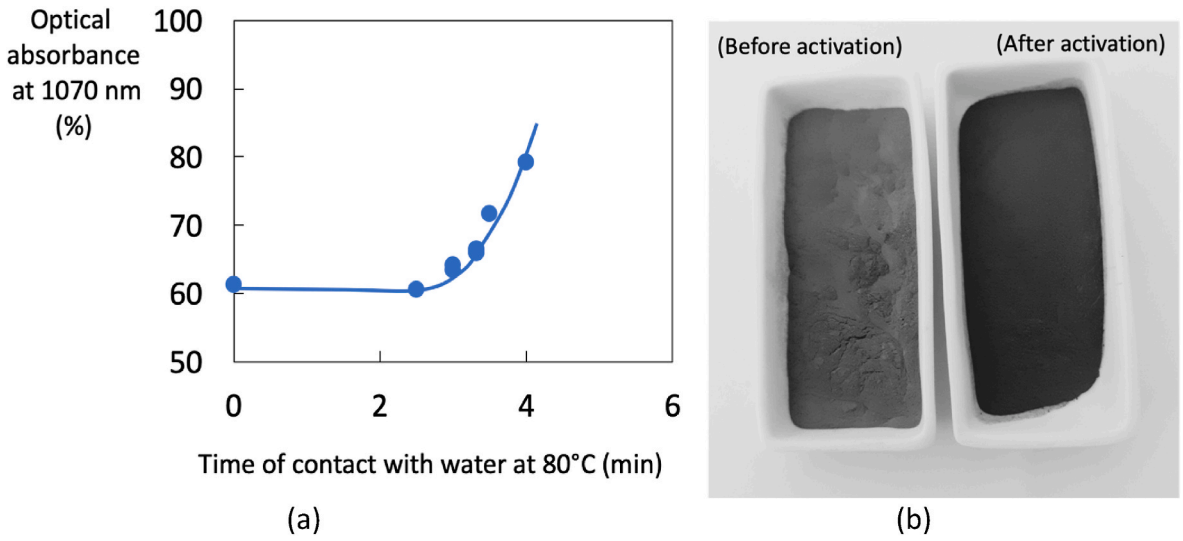

Fig. 3. (a) Optical absorption at 1070 nm of compacted powders activated for different times in water at 80 °C (concentration of AlSi12 powder in water = 400 g.L^{-1}) (b) Commercial AlSi12 powder before and after activation (photography in the visible spectral range).

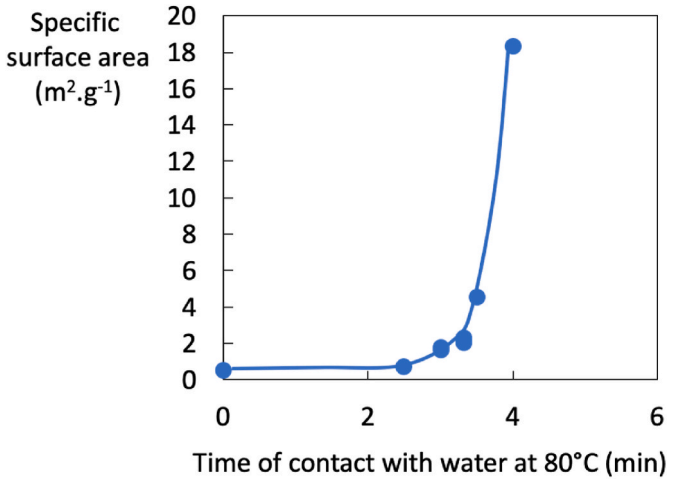

Fig. 4. Specific surface area of powders activated for different times in water at 80 °C (concentration of AlSi12 powder in water = 400 g.L^{-1}).

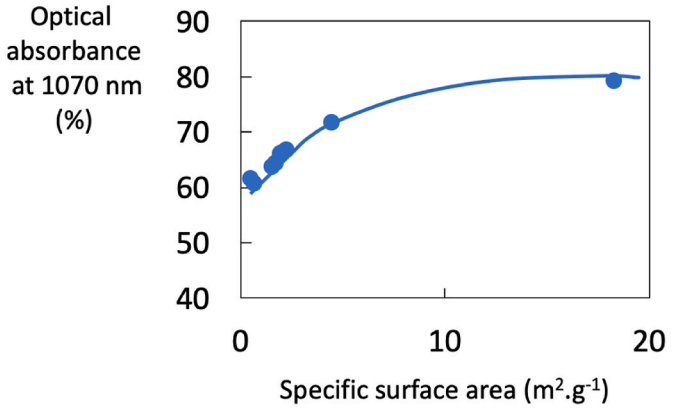

Fig. 5. Optical absorption at 1070 nm versus specific surface area for different powders activated with water.

machine, it is possible to fabricate complex ceramic-metal assemblies or periodic structures alternating ceramic and metal. Inspired by photonic [28,29], magnonic [30,31] or phononic [32] crystals, these structures could constitute new 2D or 3D metamaterials, likely to have technological applications in the field of microwave or mechanics.

2. Materials and methods

2.1. Feedstock and additive manufacturing machine

The basic feedstock was an AlSi12 powder from 3D Systems (PS2585–18) with the eutectic composition. This powder contains aluminum and silicon phases as revealed by X-ray diffraction. Such a powder is made of almost spherical particles with a median size close to 4.5 μm according to calculations made from the specific surface area (see appendix 1 equation λ). The basic feedstock was chemically treated by pure water. The process carried out is described and studied in the Result and Discussion part.

The powder bed laser fusion experiments were performed under air. A 3D Systems ProX200 machine was used. The laser beam emitted by PROX200 has a wavelength of 1070 nm and it is focused on a spot of 75 μm in diameter. Its power can be regulated from 30 to 300 W by step of 3 W.

2.2. Analytical techniques

The crystalline structure of the samples was studied using Bruker AXS D4 Endeavor diffractometer equipped with a 1D LynxEye detector. Kα radiations ($\lambda K\alpha_1 = 0.15405$ nm and $\lambda K\alpha_2 = 0.15443$ nm) emitted by a copper anode, were used as X-ray source. The Kβ ray was eliminated by a nickel filter. A second diffractometer was used (Brucker D8 Endehavior), that has a LynxEYE detector and the same wavelength as before. The X-ray source is a copper anode with the following Kα radiations: $\lambda K\alpha_1 = 0.15405$ nm and $\lambda K\alpha_2 = 0.15443$ nm. No Kβ filter is used for this device.

The microstructure of samples and patterns written by laser, were observed by optical (Optical numerical microscope VHX 1000 from Keyence) and scanning electron (Jeol JSM 6510LV) microscopes. Surface roughness analyses were carried out with Sensofar S-NEOX focused variation microscope. The chemical composition of samples was analyzed by Energy Dispersive Spectroscopy (EDS) with a Brucker Quantax electron microscope analyser. A focused ion beam combined

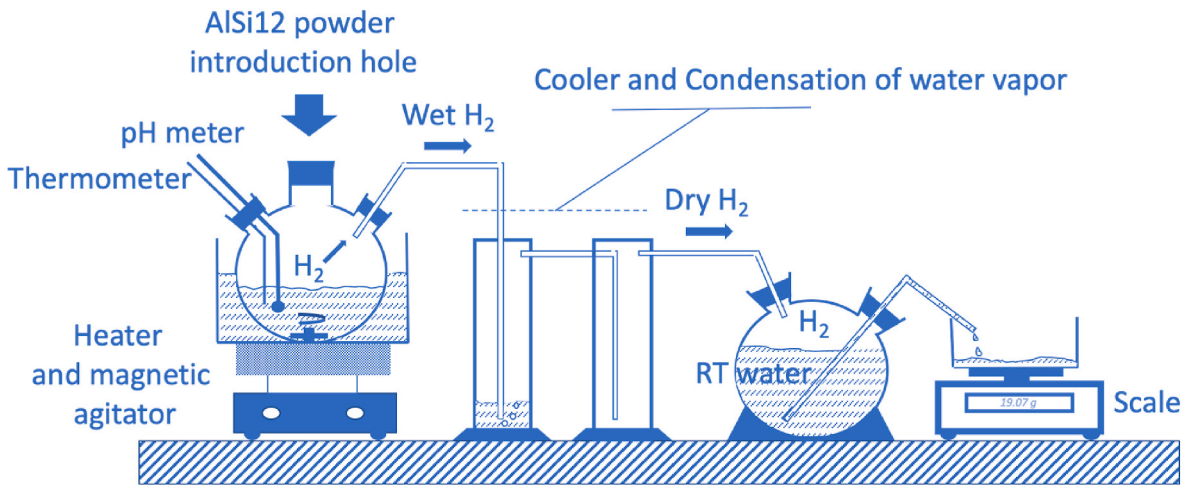

Fig. 6. Experimental setup dedicated to the measurement of hydrogen release, pH and temperature variation during the activation of AlSi12 powder.

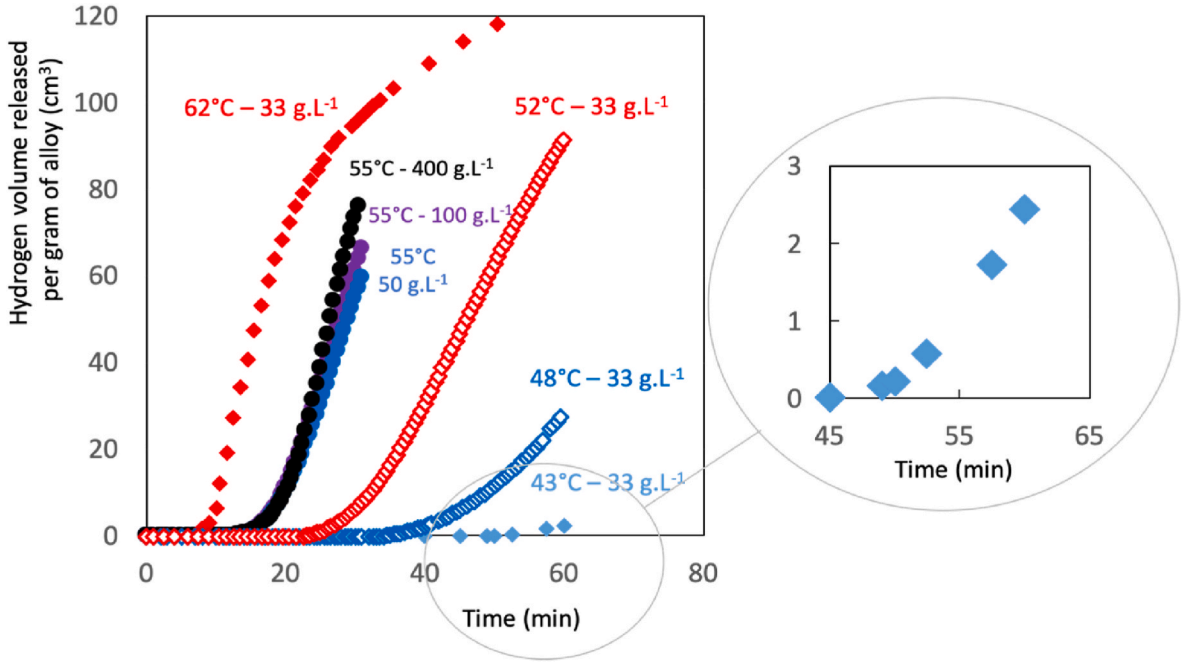

Fig. 7. Hydrogen evolution with time per 1 g of AlSi12 powder, for different water temperatures (diamonds) and concentrations of the water suspension (circles) (10 g of AlSi12 in the appropriate volume of water for the given concentrations).

with field effect emission gun (SEM/FIB FEI Helios 600i) associated with Oxford Instruments AZTEC Advanced electron microscope analyser, were used to prepare cross-sections from green pellets prepared by uniaxial compaction at 750 MPa of raw or activated metal AlSi12 powder. This equipment made it possible to carry out chemical and microstructural analyzes. Another similar system (Helios Nanolab G3UC from Thermofisher) was also used for some experiments.

The optical properties of the AlSi12 alloy powders, before and after chemical treatment, were analyzed by an Agilent Cary 5000 spectrophotometer equipped with a PbSmart NIR detector. The detection range is from 175 nm to 3300 nm. The specular mode which includes diffuse reflection and specular reflection, has been considered. Infrared spectrometry analyses were carried out between 400 and 4000 cm^{-1}, using a Nicolet 6700 apparatus from Thermofisher Scientific. The specific surface area of the powders was measured by a Tristar 3020 of Micromeritics, using the Brunauer, Emmett and Teller model (BET). The adsorbed gas was nitrogen. The density of metal and ceramic manufactured parts was measured with an Archimedes balance.

X-ray Computed tomography (CT) was carried out using a Phoenix V |tome| x M microfocus CT system from Baker Hughes. The scan was performed at 140 kV and the voxel size was 8 μm. The data was processed using Baker Hughes reconstruction software and VGSTUDIO MAX application suite (from Volume Graphics) was used for virtual cross-sections.

3. Results and discussion

3.1. Feedstock chemical treatment

As indicated in the introduction, the first objective of this work is to transform the surface of AlSI12 alloy powders with pure water. This treatment should lead to an activated powder with properties similar to those treated with sodium hydroxide [22]. Thanks to the increase of the reactivity towards oxygen and of the absorbance at the laser wavelength

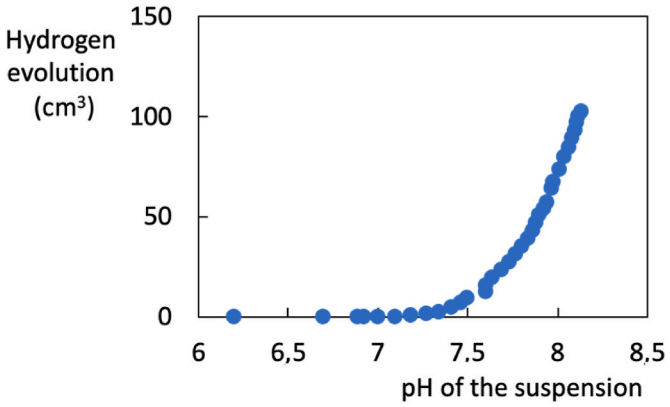

Fig. 8. Typical hydrogen evolution per 1 g of AlSi12 versus pH of the suspension (concentration of the metallic suspension in water 33 g L^{-1}, temperature 55 °C).

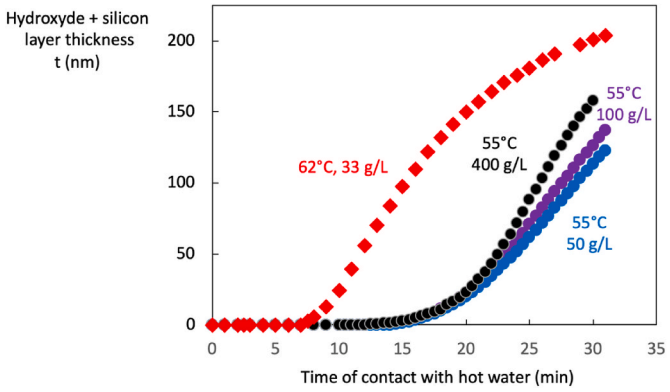

Fig. 9. Estimated average thickness t of aluminum hydroxide layer at the surface of the grains versus water contact time for different concentrations and temperatures of the suspension.

of the L-PBF process, the activated powder should then allow the manufacture under air, of parts with ceramic zones, mainly made of alumina, and metallic zones, based on AlSi12 alloy [22](Fig. 1).

The reactivity with water of the commercial AlSi12 powder (cf. Materials and Methods) was then tested. The micrometric size of its grains does not allow, at room temperature, to initiate a significant reaction with water, in agreement with the observations of Rosenband and Gany [33]. The hydrogen evolution is only observed after an initiation time in order of 10 min to nearly 1 h, depending on the water temperature. It then follows a chemical attack of the metal part which, in the case of pure aluminum, is described by the following chemical equation [24,25]:

$$2Al + 6H_2O \rightarrow 2Al(OH)_3 + 3H_2 \quad (1)$$

Due to the less reactivity of silicon, this reaction could be written as follow for AlSi12 powder (by assimilating AlSi12 to Al0.88Si0.12):

$$2Al_{0.88}Si_{0.12} + 5.28H_2O \rightarrow 1.76Al(OH)_3 + 0.24Si + 2.64H_2 \quad (2)$$

This equation is supported by microscopic observations, which reveal that metallic silicon remains inside the hydroxide aluminum layer (Fig. 2).

When the reaction is stopped even after a short time, a change in color of the dry powder is observed. The initial grey color becomes black-brown to black, depending on the progress of the activation. This change in optical absorption in the visible is also evident at the wavelength of the laser (1070 nm) used by the L-PBF process (see for instance Fig. 3). It increases significantly as a function of the progress of the activation reaction, which can thus be measured. The specific surface area of the powder also increases with time of contact with hot water (Fig. 4), because hydroxide layer formed on surface of the grains is porous. Thus, the thicker it is, the greater the overall specific surface area of the activated powder. The specific surface area can therefore characterize the progress of the activation. The values of optical absorption and specific surface area are strongly correlated as shown in Fig. 5. This also highlights that the optical absorption varies greatly for weak activations, while it tends to stabilize when the reaction is more advanced. Optical absorption is therefore only relevant for qualifying very weakly activated powders, unlike the specific surface area whose sensitivity extends over a wider domain. The optical measurement gives however information about the interaction of the laser with activated powder. The more the powder absorbs the light from the laser, the easier it will be to heat and to oxidize it.

Optical absorption at 1070 nm and specific surface area measurements, therefore make it possible to compare the activated powders with each other. They also allow to have a qualitative view of undergone modifications by AlSi12 powder grains during treatment with hot water. However, to characterize activation process more finely and to know more precisely the stages and their kinetics, as well as to quantifying the surface modifications generated, other experiments have been implemented.

A follow-up of the evolution of hydrogen, variation in pH and temperature, was carried out thanks to the setup of Fig. 6. This device has the advantage of measuring the volume of hydrogen released with a quite good precision. At room temperature, a volume of hydrogen of only 1 ml displaces a mass of 1 g of water, which is very easy to measure with a laboratory balance. Moreover, according to equation (2), 1 ml of hydrogen is generated by 3.38. 10^{-5} mol of AlSi12, i.e. 9.2. 10^{-4} g. This means that it is possible to detect the attack of less than 0.1 % of metal.

Experiments at different temperatures, using the experimental setup in Fig. 6, revealed several main results. Hydrogen is released only after an initiation period of a few minutes, regardless of the initial water temperature (Fig. 7). This period is shorter the higher the temperature. It seems reasonable to think that the initiation time of the reaction corresponds to the chemical attack of the alumina layer, which generally protects the grains of aluminum or its alloys [34–36]. The kinetics of hydrogen evolution after initiation tends logically to increase with temperature. The chemical attack of the alloy powder is even very sensitive to the temperature. For the concentration of 33 g L^{-1} of alloy in water, hydrogen is produced at 62 °C, at a rate of approximately 1.5 cm^3 min^{-1} after only 8 min, whereas at 43 °C the gas production is only 0.1 cm^3 min^{-1} after more than 45 min. These kinetics are also slightly modified by the concentration of the metallic powder in water (Fig. 7), but at 55 °C between 50 and 400 g.L^{-1}, the impact on the kinetics of the reaction is very small.

During the experiments, the exothermicity of aluminum oxidation tends to slightly increase the temperature of the alloy suspension in water. This was particularly observed for the study of very concentrated suspensions. But this temperature increase, limited to about one or two degrees for a short period of time, does not have a strong effect on the kinetics of the oxidation reaction. The pH of the metal suspension, however, seems to have a stronger influence. As shown by Fig. 8, the reaction starts above pH7.2 and is related to a continuous increase in pH. This observation tends to confirm the interpretation of Kader et al. [25], who attribute to the increase of the pH, the main role in the acceleration of the metal attack.

The quantities of aluminum transformed into aluminum hydroxide on the surface of the grains are evaluated from the measurement of the hydrogen produced (see appendix 1). The mass in grams of attacked aluminum can indeed be estimated from equation α in appendix 1, by 0.81 times the volume in liters of hydrogen produced:

$$M_{(Al\ transformed)} \simeq 0.81 V_{Hydrogen}\ (g) \quad (3)$$

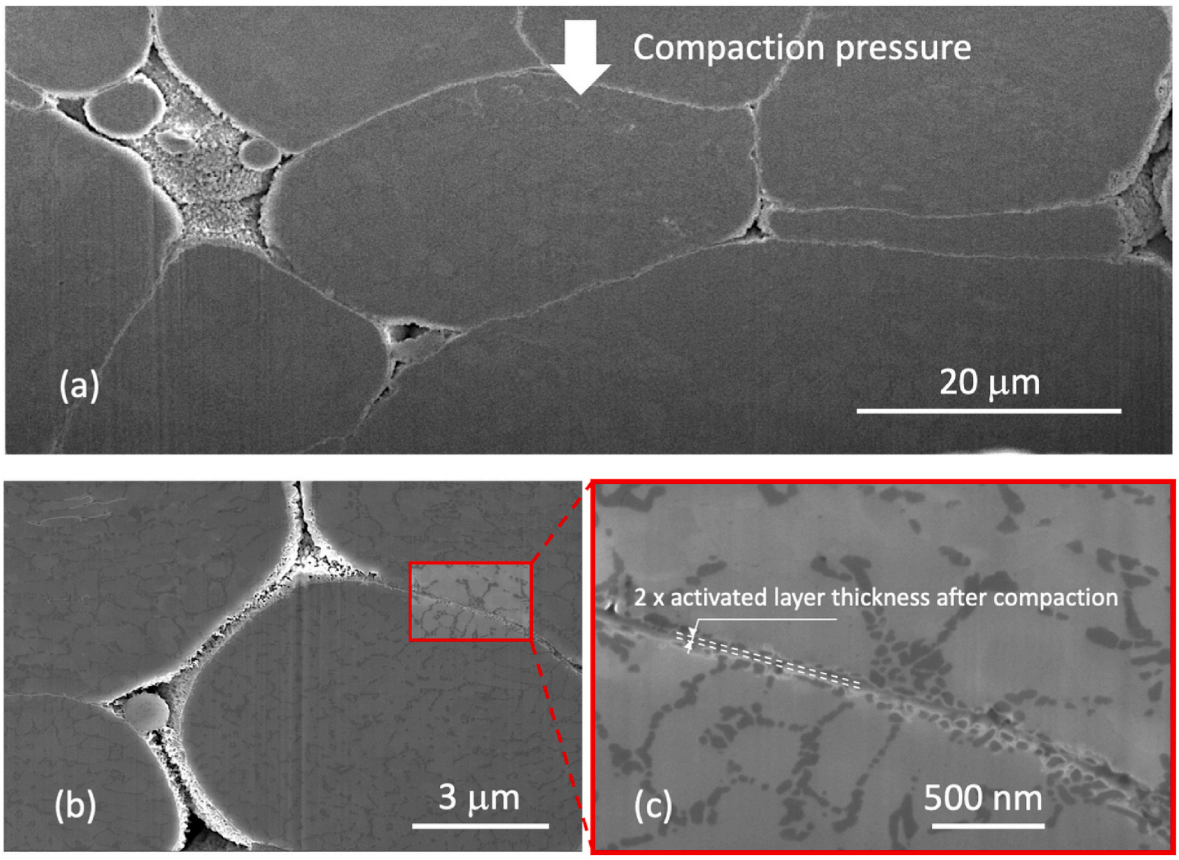

Fig. 10. Typical images obtained after cutting metallic pellets by focused ion beam:
(a) AlSi12 activated in water at 43 °C for 92 min (Sw = 7 $m^2\ g^{-1}$) the direction of compaction is according to the arrow, (b) AlSi12 activated in water at 55 °C for 15 min (Sw = 2.9 $m^2\ g^{-1}$), (c) detail of the image (b) showing the thickness of the passivation layers subjected to perpendicular pressure after compaction of the powder.

Table 1
AlSi12 powder activation conditions and main characteristics of these powders.

Sample	Activation water temperature (°C)	Activation time[a] (min)	Optical absorbance at 1070 nm (%)	Specific surface area ($m^2.g^{-1}$)
A	80	3	63 ± 2	1.9 ± 0.1
B	80	3.5	72 ± 2	4.5 ± 0.1
C	55	28	65 ± 2	2.5 ± 0.1
Ref. AlSi12	-	-	*61 ± 2*	*1.5 ± 0.1*

[a] The activation time can be defined by the contact time of the powder with the water since the powder was introduced into the reactor.

knowing that from equation (2), 1 g of attacked aluminum affects about 1.14 g of $Al_{0.88}Si_{0.12}$ alloy.

With some approximations, it is also possible to deduce the average thickness t of hydroxide layer at the surface of the grains (see appendix 1, equation ν to ο). As an illustration, estimates of the total thicknesses of the hydroxide layers and the silicon they contain, are plotted as a function of the contact time with water for several experimental conditions (Fig. 9). These thicknesses increase more strongly with increasing temperature, the concentration of the powder in the water only playing a secondary role. Experiments were also carried out at 42 °C. The results obtained have not been plotted in Fig. 9 to preserve clarity. It should be noted, however, that the hydrogen release only begins after about 50 min of contact time with water. The estimated thickness of the hydroxide layer is only about 1 nm after 1 h of experiment.

Scanning microscopy of sections obtained by FIB (see Materials and Methods), of activated powder grains, highlights the transformed surface layers (Fig. 10). Their average thickness varies according to the experimental conditions of activation, but it is lower than those observed by Veron et al. [22], which varied from 300 nm to 2 µm, depending on the sodium hydroxide concentration. This result shows that activation with water is milder than activation with sodium hydroxyde. However, in Fig. 10, it can be seen that when the grains are

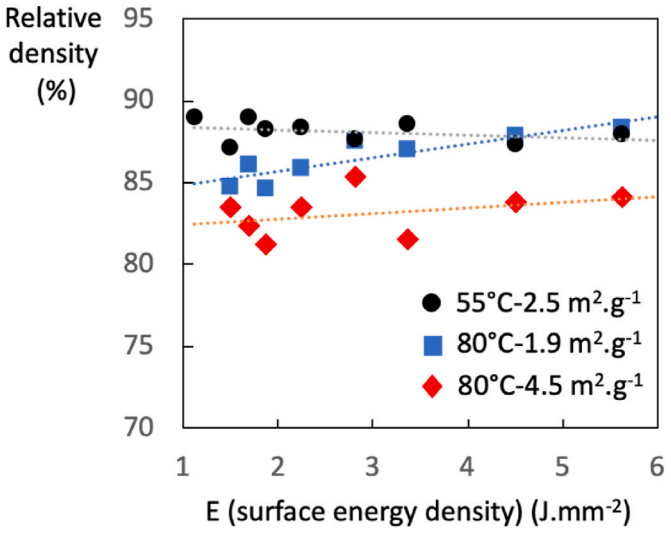

Fig. 11. Metallic sample fabricated by L-PBF process with different activated powders: relative density versus surface energy density brought by the laser.

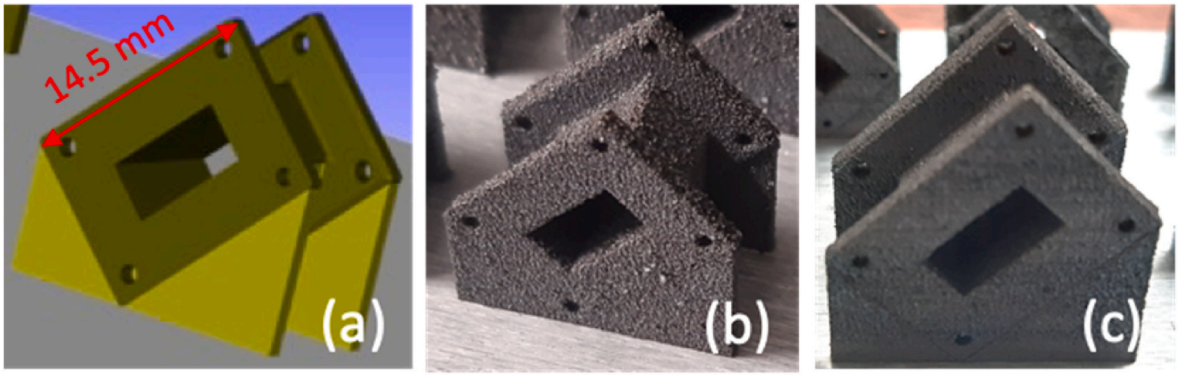

Fig. 12. Comparison of small parts made with the powder C and the reference AlSi12: a) Part design and sizing.
b) Part manufactured with activated powder.
c) Part manufactured with reference AlSi12.

Table 2
Comparison of the relative densities and the roughness of the parts made from the reference AlSi12 alloy powder and the C powder (2.5 $m^2 g^{-1}$).

L-PBF sample obtained from:	Relative density (Archimede's method) (%)	Ra (top surface) (μm)	Ra (lateral side) (μm)
AlSi12 reference	84 ± 2	28 ± 5	21 ± 8
Activated-AlSi12 (55°C-28 min)	88 ± 2	35 ± 7	32 ± 6

in contact with each other, the activated layers are compacted. They are thus thinner than in the grains whose surface, adjacent to a hole in the metal compact, is not compressed. The surface of the grains also shows a significant roughness visible on the areas cut by the FIB, as well as on the areas observed perpendicular to their surface. All these observations associated with specific surface area modifications (Fig. 4 and Table 1), confirm that the activation layer is porous. The simplifying assumption of a perfectly dense layer, used in the calculation of the average thickness (appendix 1), does not strictly correspond to reality. The calculated thicknesses (for instance 3 nm for the sample activated in water at 55 °C for 15 min and studied in Fig. 10) are thus lower than the average thicknesses measured on the electron microscopy images in the compressed zones (about 15 nm according to Fig. 10c) and, a fortiori, in the regions bordering a hole in the pellet (more than 200 nm in Fig. 10b). Some such regions are visible in Fig. 10a and b. They also show the surface roughness of the activated grains in areas with little or no compaction. The order of magnitude of the activated thicknesses obtained by calculation or evaluated from electron microscopy images being the same, the previously proposed activation mechanism seems however consistent.

Given the very low thickness of these layers, it was difficult to precisely determine their nature. For the thickest layers, analysis by IR spectrometry and X-ray diffraction confirms however, the presence of bayerite-type aluminum hydroxide.

Several 400 g batches of powders activated with pure water under different conditions, were prepared for use in the manufacture of parts, by the L-PBF process. Two main objectives were targeted:

- to demonstrate that powders weakly activated by water and free of impurities containing sodium, improve the quality of the metal parts compared to those obtained by Veron et al. [22],
- to demonstrate that obtaining ceramic-metal multi-materials parts comprising well-densified ceramic zones, is possible with these powders.

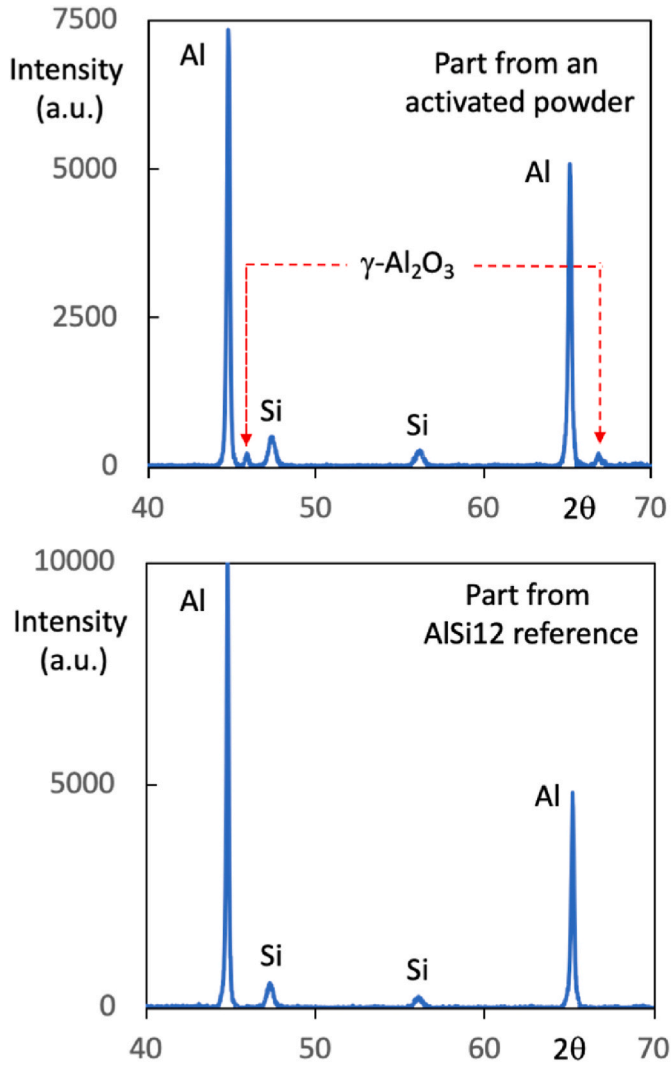

Fig. 13. Comparison of X-ray diffraction patterns for L-PBF parts coming from activated (2.5 $m^2 g^{-1}$) and reference AlSi12 powders.

It is known that unactivated powder (Specific surface area ≃ 0.5 $m^2 g^{-1}$) can produce quality metal parts by L-PBF. Therefore, to achieve the first objective, it seems preferable to activate the powder only very little. However, this activation must be "sufficient" to also be able to obtain a

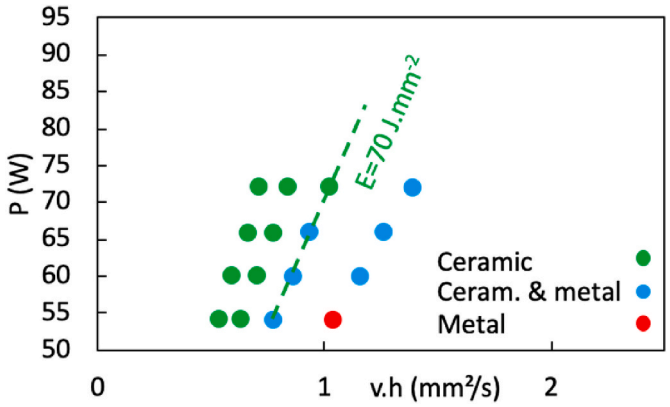

Fig. 14. Phase diagrams of samples obtained for different values of laser power P and different products of hatch spacing h and laser scanning speed v.

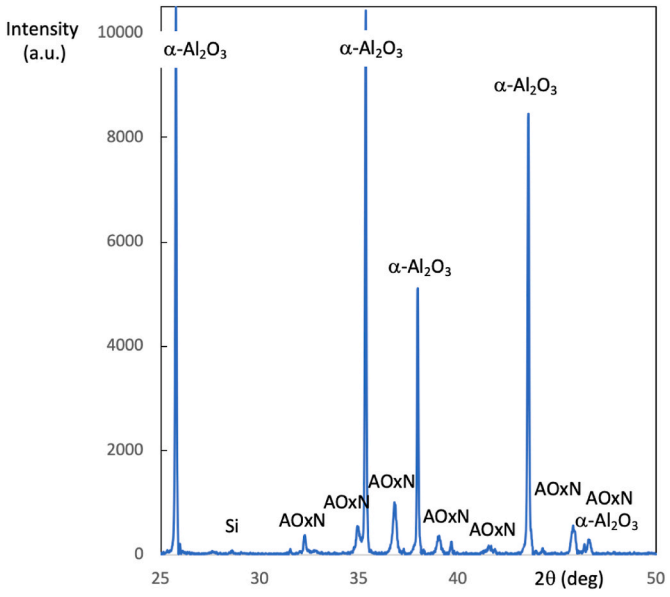

Fig. 15. X-ray diffraction pattern of a ceramic part (AOxN = Aluminum Oxide Nitride).

ceramic, with reasonable L-PBF manufacturing parameters [22]. It was therefore chosen to explore activation conditions leading to the production of powders with a moderate specific surface area, typically less than 5 $m^2\ g^{-1}$. Table 1 shows the production conditions and characteristics of the activated powders that will be used for the L-PBF process. These powders will allow the optimization of manufacturing parameters for metal parts on the one hand and ceramic parts on the other hand.

3.2. Manufactured parts by L-PBF of activated AlSi12 powders

3.2.1. Metal parts

The L-PBF process was applied to the previously selected powders. First, parallelepipedic metal parts of 10 × 10 × 8 mm^3 were prepared in order to determine the favorable conditions to obtain a well-densified, mechanically consistent material with moderate roughness. The thickness of the powder beds was set at 50 μm and the hatch spacing at 100 μm, standard values for the used AlSi12 alloy powders. On the other hand, the laser power and the scanning speed were adjusted to values from 54 to 225 W and 100–1200 mm s^{-1}, respectively. The results obtained are presented in a synthetic way (Fig. 11) by the evolutions of the relative density, as a function of the surface energy density E ($J.mm^{-2}$) brought by the laser. This surface energy density is defined by:

$$E = \frac{P}{v.h} \quad (4)$$

with P the laser power, v the scanning speed and h the hatch spacing.

It should be noted that below a laser power of approximately 60 W and even 90 W when scanning speeds are high (greater than or equal to 800 mm s^{-1}), a coherent part cannot be obtained. The very synthetic Fig. 11 does not show this result, which must however, be considered.

Fig. 11 shows that the best densifications are obtained for the lowest activated powders (A and C in Table 1), with specific surfaces areas of the order of 2 $m^2\ g^{-1}$, to which a surface energy density between 1 and 2.5 J mm^{-2} has been applied. Stronger activation indeed, leads to a higher specific surface area which reflects a greater quantity of hydroxide formed. During laser exposure, this hydroxide transforms into oxide, which tends to prevent the sintering of the metal particles, because of wettability problems encountered in different metal-ceramic interfaces [37]. For similar reasons, the hydroxide phase is also responsible for an increase in surface roughness. We chose to select the activated powder C(55 °C, 2.5 $m^2\ g^{-1}$) for the rest of the work. The best arithmetic roughness that it allows to reach is certainly a little higher than those obtained with the powder A (Ra = 35 against 25 μm), but the relative densities to which it allows to reach, are higher. Moreover, its greater specific surface area (2.5 against 1.9 $m^2\ g^{-1}$) will be more favorable to the oxidation of the metal, necessary for the formation of the ceramic.

The precise additive manufacturing conditions used for this powder are then as follows:

- Laser power P: 135 W
- Scanning speed v: 800 mm s^{-1}
- Hatch spacing: 100 μm

Using these conditions, the activated powder produces parts with a quality approaching that made with conventional AlSi12 powder, as shown in Fig. 12 and the data collected in Table 2. X-ray diffraction (Fig. 13) also shows that parts made from pure water-activated powder, with a surface area of 2.5 $m^2\ g^{-1}$, are predominantly aluminum and silicon, from the eutectic AlSi12 alloy, as with parts obtained with commercial AlSi12. A very minor secondary phase is present, however, in the parts derived from the activated powder, as revealed by two additional small peaks. These peaks are attributed to the (400) and (440) diffraction planes of γ-Al_2O_3 oxide (see JCPDS reference n° 00-010-0425). It is not surprising that the temperature rise during laser melting, leads to the formation of an aluminum oxide by dehydration of the hydroxide layer formed on the surface of the particles. The chemical reaction involved is simply:

$$2Al(OH)_3 \rightarrow Al_2O_3 + 3H_2O \quad (5)$$

However, the stabilization of the gamma variety of aluminum oxides, which usually occurs only as a high surface-to-volume ratio material, was not expected. The existence of strong mechanical stresses in the manufactured parts is very probably at the origin of the stabilization of this metastable phase.

Despite the few differences observed between the parts from activated or commercial powders, we can therefore conclude at this stage, that the first objective set in part 3.1 has been achieved.

We note that the relative density of 88 % for parts made from an activated powder remains low. The formation of oxide and hydrogen bubbles during the decomposition of water resulting from the dehydration of the hydroxide on the grain surface, are most likely responsible for the residual porosity. To reduce it, dehydration of the hydroxide of the raw material in the form of boehmite AlO(OH) or aluminum oxide, would have to be implemented. Conventional annealing or sintering by Spark Plasma Sintering could also rectify this defect, however affecting the initial dimensions of the part.

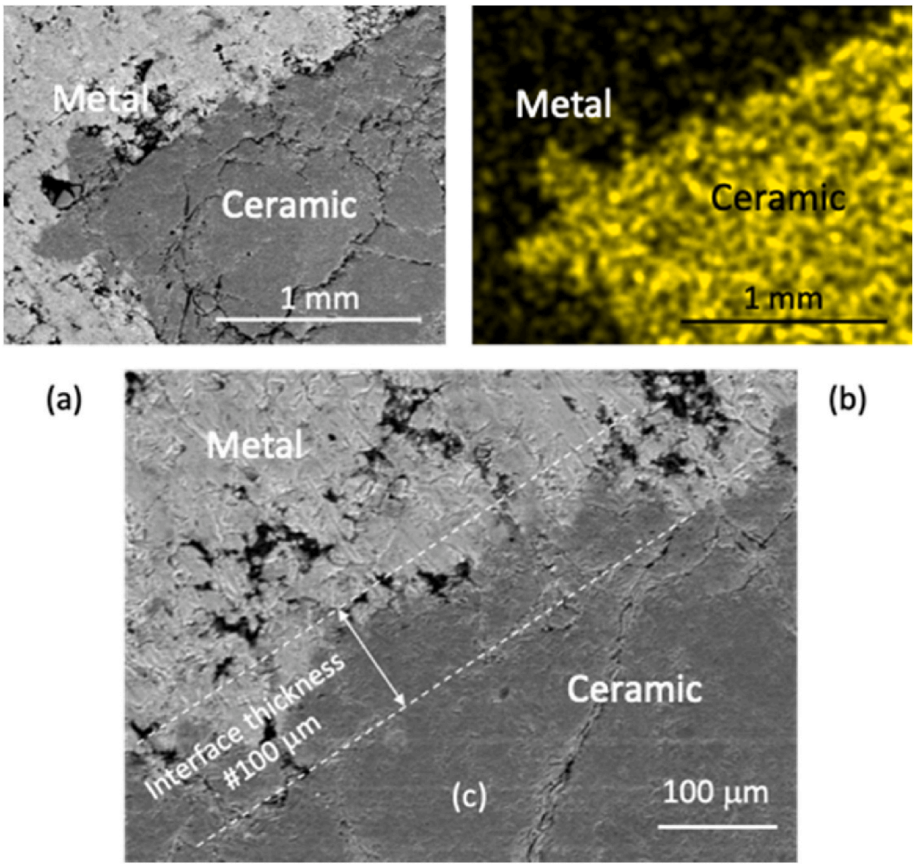

Fig. 16. Ceramic-metal interface: (a) and (b) General view and corresponding oxygen mapping of the corner of a ceramic square surrounded by metal; (c) Detail of the interface and evaluation of the thickness of the ceramic and metal interpenetration area.

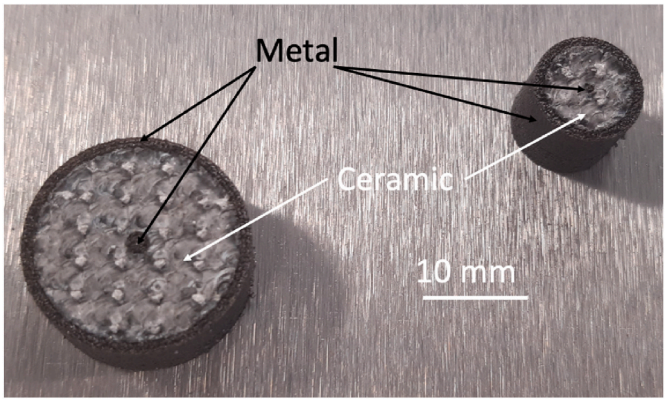

Fig. 17. Image of a coaxial conductor made by L-PBF with a powder activated by pure water at 55 °C.

3.2.2. Ceramic parts

In order to achieve the second objective displayed in section 3.1, more energetic manufacturing conditions were applied to the activated powder, in order to ensure its oxidation and sintering into a properly densified ceramic. This approach was dictated by the pioneering work of Veron et al. [22] who had however, practiced sodium hydroxide activation, which was much more severe than that implemented in the present work. Samples of 7 × 7x4 mm^3 surrounded by 1.5 mm of metal and resting on 4 mm thick a metal base, were therefore fabricated with different P, v and h. Phase diagrams P = f(v.h) were plotted (Fig. 14) to summerize the results of the different test arrays.

For high powers and low v.h products, i.e. for high surface energy densities, oxide and oxide nitride are mainly obtained. These are corundum alumina (α-Al_2O_3, JCPDS file n° 01-089-3072(C)) and aluminum oxide nitride (4AlN–96Al_2O_3, JCPDS file n° 00-020-0043 (N)) in which traces of metallic silicon may remain (Fig. 15). The alumina phase is predominant, but the severe heating conditions during manufacturing allow a partial reaction of nitrogen in the air, with aluminum. In the resulting oxide-nitride, however, nitrogen is a very minor constituent compared to oxygen.

Starting from the oxide zone (Fig. 14) and moving in the diagram along a diagonal from the upper left corners to the lower right corners, one encounters a zone in which alumina and metal alloy can coexist, and then a zone in which only metal is identified. In contrast to the observations made by Veron et al. in experiments with sodium hydroxide activated powders, the transitions between the ceramic and metallic zones are therefore less abrupt. Moreover, the boundary separating these zones corresponds to a line of higher energy densities (about 70 J mm^{-2}) than during sodium hydroxide activation (36 J mm^{-2} [22]). This result was expected since water activation is weak and therefore, cannot have the same oxidation-facilitating effect as sodium hydroxide activation.

3.2.3. Ceramic-metal multi-materials and « metamaterials »

The process implemented to produce the metal or ceramic parts, as described above, is obviously very interesting for the production of multi-material parts. It is all the more interesting as it opens the way to the manufacturing of parts comprising at least two different materials deposited at will, in the three directions of space, using only the L-PBF technology and a single feedstock.

Thermal cycling tests were performed on such multi-materials between −55 °C and +125 °C with heating and cooling rates of 2 °C/min and intermediate holding times of 15 min. They revealed no crack

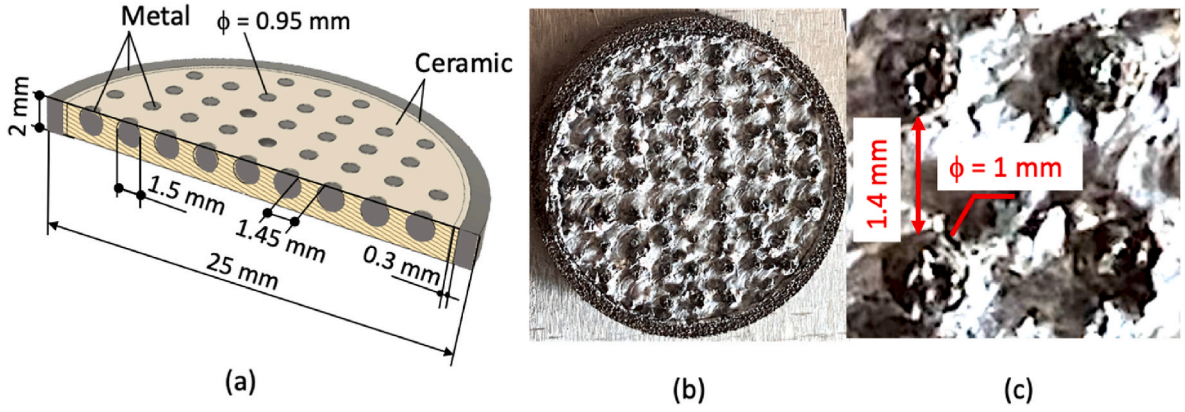

Fig. 18. Schematic section of the fabricated bi-material
part (a), view of the real part in a direction perpendicular to the manufacturing plane (b), detail of the surface of the real part (c).

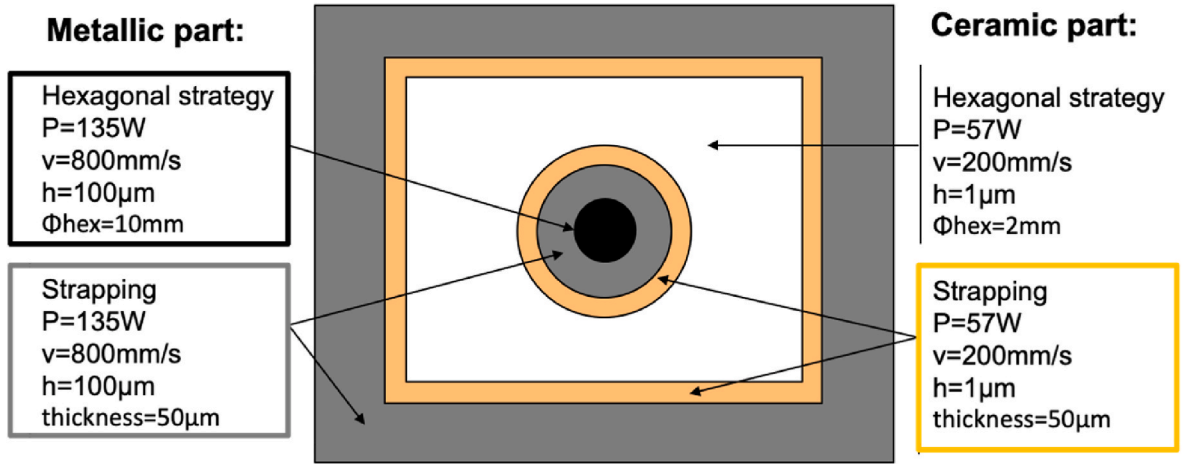

Fig. 19. Schematic representation of manufacturing parameters and strategies used for ceramic parts comprising a single layer of metal spheres, distributed in a square planar array.

propagation, even after 200 cycles. The cohesion between these materials with very different characteristics, in particular their expansion coefficient, is thus strong. To date, however, a more in-depth study intended to demonstrate by electron microscopy, the development of dislocations or other modifications at the scale of atomic rows, has not been carried out.

The cohesion between the ceramic and the metal seems ensured by an "entangled" interface over a thickness of approximately 100 µm as shown in Fig. 16. In addition, during the construction of the ceramic areas of the parts, oxidation cannot stop sharply at the interface with the metal. There is necessarily a narrow band in which a metal-ceramic composite exists. The latter certainly allows a progressive accommodation of the expansion coefficients of ceramics and metal. This zone therefore also contributes to preserving the interfaces and avoiding the propagation of cracks that thermomechanical shocks could cause, given that metal has an expansion coefficient approximately three times greater than that of ceramic (α ceramic # 8 K^{-1}, α AlSi12 # 22 K^{-1}).

However, this progressive and tangled interface, could be a drawback for some technological applications requiring sharper transitions between two materials. The components for microwave electronics, a priority technological application, could potentially be concerned. It will therefore be necessary in the future to adapt the manufacturing conditions in these interfacial areas to find the best compromises.

Using the developed process, it was possible to fabricate coaxial structures enclosing a conductive core in a ceramic, itself surrounded by metal (Fig. 17). All the fabricated devices conducted electricity through the sample (10 mm thick) in their central and peripheral part. Despite the color differences observed in the ceramic block due to some silicon precipitates, no electrically conductive areas were found in it. The dielectric character and its homogeneity within the ceramic were therefore satisfactory.

The process studied in this work has also favored the construction of even more complex structures, including a 2D and especially 3D periodicity, to get closer to the realization of metamaterials. This was done on small centimeter parts. Ceramic parts encircled with metal were thus built with metallic spheres placed periodically inside. These spheres were either 1.5 or 2 mm in diameter and were flush with the ceramic surface as shown in Fig. 18 for the case of 1.5 mm spheres. The truncation of each sphere presented on the surface of the ceramic, is a disc of the order of 1 mm in diameter. The detailed fabrication conditions of these parts are given in a schematic (Fig. 19). A hexagonal strategy was used to fabricate the majority of the ceramic and metallic parts. Two hoops, one ceramic and one metallic, were constructed to ensure the geometric shape of the samples.

The real part obtained (Fig. 18b) presents a rather high surface roughness (Ra >80 µm). However, the small metal balls that are flush with the ceramic are clearly visible. According to the construction file (Fig. 18a), the flush metal discs should have a diameter of 0.94 mm and be 1.45 mm apart. On the real part, we find very close values (Fig. 18c), which demonstrate the good conformity of the fabricated metal-ceramic structure, with the digital file. On the other hand, the high surface roughness does not allow to clearly observe the circular geometry of the

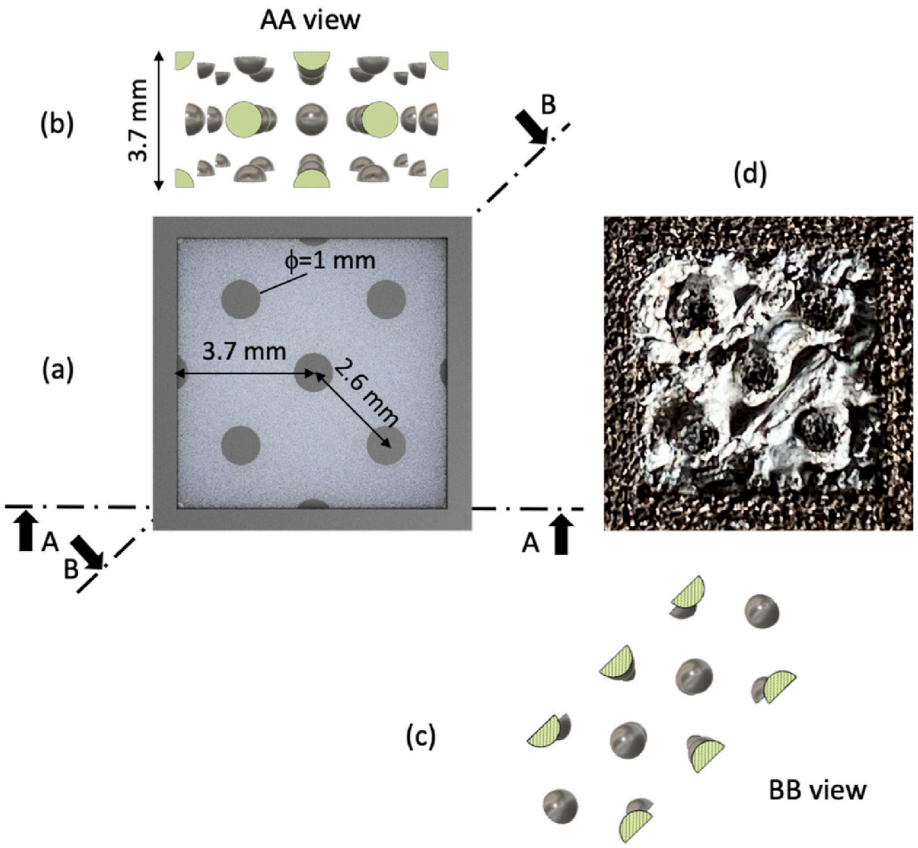

Fig. 20. Representation of the manufactured bi-material part (a) associated with two cross-sectional views of the metal balls inserted into the ceramic matrix (b) and (c).
View of the actual part at the same scale,
in a direction perpendicular to the manufacturing plane (d).

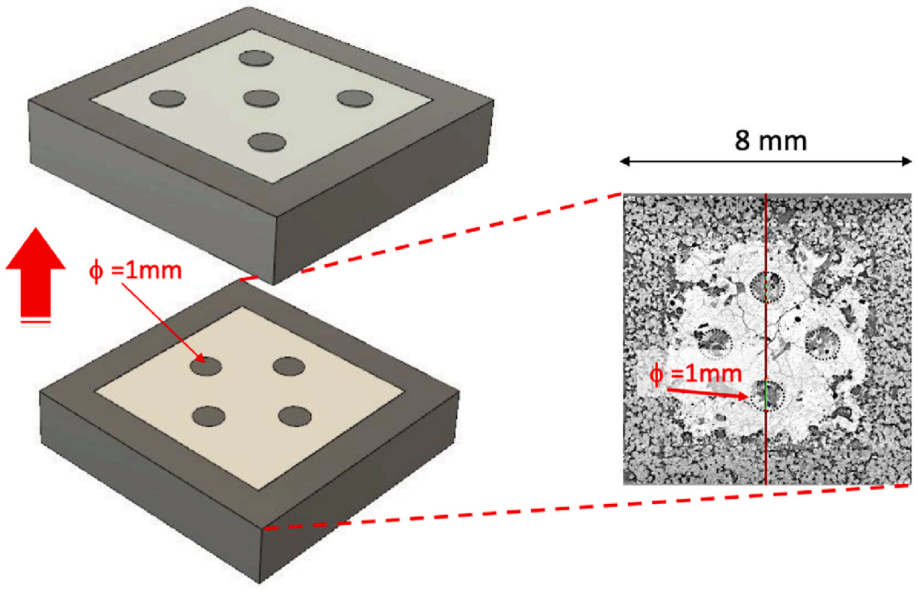

Fig. 21. X-ray tomography of a part comprising a face-centered cubic arrangement of metallic spheres embedded in an alumina-based ceramic. The section observed by tomography corresponds to the plane of the balls completely embedded in the ceramic part (see Fig. 20).

metal discs section, as drawn in Fig. 18a.

Using similar conditions, other ceramic parts, this time consisting of three superimposed layers of metallic spheres or half-spheres of 1 mm diameter, were fabricated. The arrangement of the metallic entities is face-centered cubic symmetry (Fig. 20). The metal spheres truncated by half are clearly visible on the real part (Fig. 20d). However, they are again embedded in a ceramic with a high roughness (Ra >80 μm). X-ray tomography allows us to observe the metallic inclusions located in the

core of the ceramic piece (Fig. 21). However, this observation is disturbed by the presence of some silicon precipitates whose X-ray contrast is similar to that of the AlSi12 alloy. The geometric arrangement and overall dimensions of the "buried" metallic features are consistent with the digital object. Differences in dimensions of less than a tenth of a millimeter, have been observed in the (x,y) plane. It should be noted, however, that the spherical metallic entities are not perfectly fabricated. The ceramic seems to have penetrated these porous spheres. Although they are inscribed in a circle, their sections revealed by the tomography, are thus jagged, (Fig. 21).

There is still progress to be made to improve the geometric quality of surfaces and interfaces. An improvement will notably involve the search for more efficient laser exposure strategies (contours of ceramic or metal zones, local reflows, compaction of powder beds, etc.). Because powders play a key role in the quality of parts obtained by laser fusion, other powder particle sizes could also be advantageously used.

Microwaves extend from 300 MHz to 300 GHz, i.e. between wavelengths (in vacuum or air) of about 1 m to 1 mm. The three-dimensional periodic metal patterns, realized on a millimeter scale in a dielectric ceramic matrix, thus give hope for the future realization of real 3D metamaterials, useable in a large part of the microwave domain. However, a considerable amount of work remains to be done to achieve truly functional metamaterials. The construction strategy of the metallic inserts must indeed be better mastered so that they have very well-defined geometries and that their density is high. It will also be necessary to define precisely by calculation, the periodic structures or particular architectures interesting for a given spectral range, to realize them by the developed L-PBF process and to test in real operating conditions, the manufactured parts.

4. Conclusion

The proposed L-PBF process allows the fabrication or parts comprising, in selected areas of the space, a ceramic or a metallic alloy from a single powder chemically activated by pure hot water. Three main phases condition the successful manufacture of multi-material parts by this process:

- the chemical activation of the starting alloy powder,
- the fusion and densification of metallic zones,
- the oxidation and sintering for ceramic zones.

Each of these phases has been studied and has been the subject of initial improvements. The chemical activation has been controlled in order to obtain powders allowing both the correct fusion of the metallic zones and the oxidization of the activated powder and sintering for the ceramic zones. The L-PBF parameters were also adjusted to take full advantage of the activated powders.

The results obtained allowed to approach the realization of functional multi-material structures. Thus, small coaxial conductors have been fabricated. Beyond these relatively simple parts, periodic metal-ceramic structures (2D and 3D) have been successfully built. Even if the geometrical regularity and the density of the metallic entities included in the ceramic still need to be improved, the scales of size and periodicity that can be reached by the implemented process, seem to open the way to the subsequent fabrication of metamaterials for microwave applications.

Declaration of competing interest

The authors declare the following financial interests/personal relationships which may be considered as potential competing interests: No

Acknowledgments

The authors would like to thank Marie-Claire Barthélémy, Vincent Baylac, Yann Borjon-Piron at Cirimat for their help in surface area measurements, additive manufacturing support and logistic, and for the microscopy observations. They also thank Patrick Nguyen from Elemca for its technical support with the focused ion beam preparations. They are also grateful for the advice and experimental help provided by Yohann Thimont and Diane Samelor (Cirimat) for the optical measurements.

Appendix 1

$Al_{0.88}Si_{0.12}$: calculation of the thickness of the transformed layer at the periphery of the grains after activation by water

Table 1
Definition of the main variables used:

Variable	Definition
D	Average diameter of the AlSi12 grains of powder (in μm)
e	Cumulative thickness of the degraded aluminum layer and of the silicon trapped in this layer (in μm)
M	Mass of the studied AlSi12 alloy sample (in g)
v_A	Volume of aluminum transformed (in liter)
v_S	Volume of silicon trapped in the hydroxide layer (in liter)
V_{H_2}	Volume of hydrogen released (in liter)
t	Total thickness of the transformed layer

Assumption : *Si is not oxidized in* $Al_{0.88}Si_{0.12}$, *the equation* (1) *in the article becomes*:

$$2Al_{0.88}Si_{0.12}+5.28H_2O\rightarrow 1.76Al(OH)_3+0.24Si+2.64H_2 \quad (2a)$$

M = *Mass of the test sample* $Al_{0.88}Si_{0.12}$ (*in g*); V_{H_2} = *released hydrogen* (*liter*)

$\frac{V_{H_2}}{22.4}$ = *number of moles of hydrogen*

is related from eq.(2) *to* $0.88.\frac{2}{2.64}.\frac{V_{H_2}}{22.4} = 0.03.V_{H_2}$ *moles of transformed Al*

and $0.12.\frac{2}{2.64}.\frac{V_{H_2}}{22.4} = 0.004.V_{H_2}$ *moles of remaining metallic Si*

For V_{H_2} *released*,

the mass of Al transformed into hydroxyde is:

$$0.88.\frac{2}{2.64}.\frac{V_{H_2}}{22.4}.Al\ atomic\ mass = 0.03\ .\ 27.V_{H_2} = 0.81.V_{H_2}(g) \quad \text{(eq. α)}$$

the mass of remaining metallic Si:

$$0.12.\frac{2}{2.64}.\frac{V_{H_2}}{22.4}.Si\ atomic\ mass = 0.004\ .\ 28.V_{H_2} = 0.112.V_{H_2}(g) \quad \text{(eq. β)}$$

The corresponding volumes are then:

$$for\ Al\ transformed: v_A = \frac{0.81.V_{H_2}}{volumic\ mass\ of\ Al} = \frac{0.81.V_{H_2}}{2.7} = 0.3V_{H_2} \quad \text{(eq. γ)}$$

$$for\ remaining\ metallic\ Si: v_S = \frac{0.112.V_{H_2}}{volumic\ mass\ of\ Si} = \frac{0.112.V_{H_2}}{2.33} = 0.048.V_{H_2} \quad \text{(eq. δ)}$$

The volume fraction of transformed Al and remaining metallic Si compared to the total volume V of $Al_{0.88}Si_{0.12}$ *is*:

$$\frac{v_A + v_S}{V} = \frac{volumic\ mass\ of\ AlSi12}{M}.(0.3V_{H_2} + 0.048.V_{H_2})$$

$$= \frac{2.65}{M}.\ 0.348.V_{H_2} = 0.922.\frac{V_{H_2}}{M} \quad \text{(eq. ε)}$$

If $D(\mu m)$ *is the average grain diameter, the average volume of an* $Al_{0.88}Si_{0.12}$ *grain in* μm^3 *is*:

$$\frac{4}{3}\pi\left[\frac{D}{2}\right]^3 \quad \text{(eq. ζ)}$$

If e = *thickness of transformed Al* + *remaining metallic Si*,

$$the\ corresponding\ volume\ in\ a\ grain\ is:\ \frac{4}{3}\pi\left[\left[\frac{D}{2}\right]^3 - \left[\frac{D-2e}{2}\right]^3\right] \quad \text{(eq. η)}$$

This volume is equal to the fraction of the degraded $Al_{0.88}Si_{0.12}$ *multiplied by the volume of the grain, that gives*:

$$\frac{4}{3}\pi\left[\left[\frac{D}{2}\right]^3 - \left[\frac{D-2e}{2}\right]^3\right] = 0.922.\frac{V_{H_2}}{M}.\frac{4}{3}\pi\left[\frac{D}{2}\right]^3 \quad \text{(eq. θ)}$$

From the previous equation $e(\mu m)$ *can be calculated*:

$$e = \frac{D}{2} - \frac{D}{2}\left(1 - 0.922.\frac{V_{H_2}}{M}\right)^{\frac{1}{3}} \quad \text{(eq. ι)}$$

The average grain diameter D, *if the grains are assumed to be spherical, can be calculated from the specific surface area of the powder*:

$$Specific\ surface\ area = \frac{6}{\rho\ of\ AlSi12.D} \quad \text{(eq. κ)}$$

$$D = \frac{6}{\rho\ of\ AlSi12\ .Specific\ surface\ area} = \frac{6}{(2.65.10^6).(0.5)} = 4.510^{-6}m = 4.5\mu m \quad \text{(eq. λ)}$$

That gives:

$$e = 2.25 - 2.25\left(1 - 0.92.\frac{V_{H_2}}{M}\right)^{\frac{1}{3}} \quad \text{(eq. μ)}$$

Remarks:
$e = 0$ *when the grain is not degraded* $(V_{H_2} = 0)$,
e is close to the radius of the grain when the grain is totally transformed
i.e for $V_{H_2} = 1.09$ *liter and* $M = 1g$
in agreement with the chemical equation(2):

$$2Al_{0.88}Si_{0.12} + 5.28H_2O \rightarrow 1.76Al(OH)_3 + 0.24Si + 2.64H_2 \quad (2b)$$

According to eq (2), 1 cm^3 *of* $Al_{0.88}Si_{0.12}$ *gives about* $3cm^3$ of hydroxide and silicon, assuming that the starting $Al_{0.88}Si_{0.12}$ alloy has a molar mass of 27 g and a density of 2.65 g cm^{-3} on the one hand, and the hydroxide and the metallic silicon resulting from the activation reaction, have an atomic mass and a density close respectively to 78 g and 2.4 g cm^{-3} for the hydroxide and 28 g and 2.33 g cm^{-3} for the silicon, on the other hand. Assuming perfect dense layers and t is the thickness of the hydroxide and silicon layer, the ratio "Volume of hydroxide layer/Volume of degraded alloy layer" is such that:

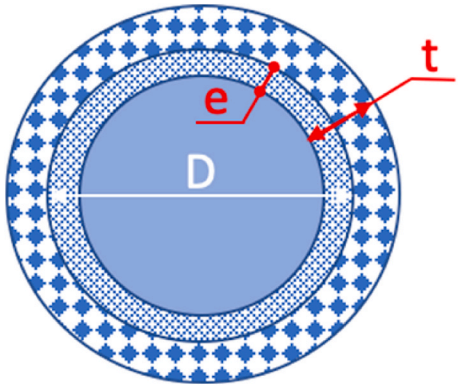

$$\frac{\frac{4}{3}\pi\left[\left[\frac{D+2t-2e}{2}\right]^3-\left[\frac{D-2e}{2}\right]^3\right]}{\frac{4}{3}\pi\left[\left[\frac{D}{2}\right]^3-\left[\frac{D-2e}{2}\right]^3\right]}=3 \quad \text{(eq. } \nu\text{)}$$

$$\Longleftrightarrow \frac{t}{e}.\frac{\left(4t^2+6t(D-2e)+3(D-2e)^2\right)}{\left(4e^2-6De+3D^2\right)}=3 \quad \text{(eq. } \xi\text{)}$$

When e ≪ D and t ≪ D (i.e.for low water activation),

$$\textit{typically for } t \geq e \textit{ and } t \textit{ and } e < \frac{D}{50}, \textit{we have}: \frac{\left(4t^2+6t(D-2e)+3(D-2e)^2\right)}{\left(4e^2-6De+3D^2\right)} \rightarrow 1$$

that gives: $\boldsymbol{t \simeq 3e}$ (eq. o)

The real **hydroxide layer observed by electron microscopy, would then be close to 3e** if it is perfectly dense or thicker if it is porous.

References

[1] Yap CY, Chua CK, Dong ZL, Liu ZH, Zhang DQ, Loh LE, et al. Review of selective laser melting: materials and applications. Appl Phys Rev 2015;2:041101. https://doi.org/10.1063/1.4935926.

[2] Rafiee M, Farahani RD, Therriault D. Multi-material 3D and 4D printing: a survey. Adv Sci 2020;1902307:1–26. https://doi.org/10.1002/advs.201902307.

[3] Yu WH, Sing SL, Chua CK, Kuo CN, Tian XL. Particle-reinforced metal matrix nanocomposites fabricated by selective laser melting: a state of the art review. Prog Mater Sci 2019;104:330–79. https://doi.org/10.1016/j.pmatsci.2019.04.006.

[4] Koopman J, Voigt J, Niendorf T. Additive manufacturing of a steel-ceramic multi-material by selective laser melting. Metall Mater Trans B 2019;50(2):1042–51. https://doi.org/10.1007/s11663-019-01523-1.

[5] Pasquet I, Baco-Carles V, Chamelot P, Gibilaro M, Massot L, Tailhades P. A multi-material based on metallic copper and spinel oxide made by powder bed laser fusion: a new nanostructured material for inert anode dedicated to aluminum electrolysis. J Mater Process Technol 2020;278:116452. https://doi.org/10.1016/j.jmatprotec.2019.116452.

[6] Zhang B, Jaiswal P, Rai R, Nelaturi S. Additive manufacturing of functionally graded material objects: a review. J Comput Inf Sci Eng 2018;18(4):041002. https://doi.org/10.1115/1.4039683.

[7] Stichel Th, Laumer T, Linnenweber T, Amend Ph, Roth S. Mass flow characterization of selective deposition of polymer powders with vibrating nozzles for laser beam melting of multi-material components. Phys Procedia 2016;83:947–53. https://doi.org/10.1016/j.phpro.2016.08.099.

[8] Anstaett Ch, Seidel Ch. Multi-Material Processing. Next step in laser-based powder bed fusion. Laser Technik J. 2016;4:28–31. https://doi.org/10.1002/latj.201600027.

[9] Wei Ch, Li L. Recent progress and scientific challenges in multimaterial additive manufacturing via laser-based powder bed fusion. Virtual Phys Prototyp 2021;16(3):347–71. https://doi.org/10.1080/17452759.2021.1928520.

[10] Andriani C. Review on melting of multiple metal materials in additive manufacturing. In: Proceedings of the International Conference on Progress in Additive Manufacturing; 2014. p. 139–44. https://doi.org/10.3850/978-981-09-0446-3.

[11] Al-Jamal OM, Hinduja S, Li L. Characteristics of the bond in Cu-H13 tool steel parts fabricated using SLM. CIRP Ann 2008;57(1):239–42. https://doi.org/10.1016/j.cirp.2008.03.010.

[12] Benning MJ, Dalgarno K. Proof of concept of a novel combined consolidation and transfer mechanism for electrophotographic 3D printing. Rapid Rapid Prototyping J 2018;24(6):1040–8. https://doi.org/10.1108/RPJ-04-2018-0111.

[13] Neirinck B, Li XS, Hick M. Powder deposition systems used in powder bed-based multimetal additive manufacturing. Acc Mater Res 2021;2(6):387–93. https://doi.org/10.1021/accountsmr.1c00030.

[14] Aerosint: https://aerosint.com/.

[15] Wei Ch, Li L, Zhang X, Chueh YH. 3D Printing of multiple metallic materials via modified selective laser melting. CIRP Annals 2018;67(1):245–8. https://doi.org/10.1016/j.cirp.2018.04.096.

[16] Mussatto A, Groarke R, Vijayaraghavan RK, Obeidi MA, MacLoughlin R, McNally PJ, et al. Laser-powder bed fusion in-process dispersion of reinforcing ceramic nanoparticles onto powder beds via colloid nebulization. Mater Chem Phys 2022;287:126245. https://doi.org/10.1016/j.matchemphys.2022.126245.

[17] Kusoglu IM, Gökce B, Barcikowski S. Research trends in laser powder bed fusion of Al alloys within the last decade. Addit Manuf 2020;36:101489. https://doi.org/10.1016/j.addma.2020.101489.

[18] Lathabai S. Additive manufacturing of aluminium-based alloys and composites. Elsevier Ltd; 2018. https://doi.org/10.1016/b978-0-08-102063-0.00002-3.

[19] Aboulkhair NT, Simonelli M, Parry L, Ashcroft I, Tuck C, Hague R. 3D printing of aluminium alloys: additive manufacturing of aluminium alloys using selective laser melting. Prog Mater Sci 2019;106:100578. https://doi.org/10.1016/j.pmatsci.2019.100578.

[20] Minasyan T, Hussainova I. Laser powder-bed fusion of ceramic particulate reinforced aluminum alloys: a review. Materials 2022;15:2467. https://doi.org/10.3390/ma15072467.

[21] Goll D, Schuller D, Martinek G, Kunert T, Schurr J, Sinz C, et al. Additive manufacturing of soft magnetic materials and components. Addit Manuf 2019;27:428–39. https://doi.org/10.1016/j.addma.2019.02.021.

[22] Veron F, Lanoue F, Baco-Carles V, Kiryukhina K, Vendier O, Tailhades Ph. Selective laser powder bed fusion for manufacturing of 3D metal-ceramic multi-materials assemblies. Addit Manuf 2022;50:102550. https://doi.org/10.1016/j.addma.2021.102550 video at. https://www.youtube.com/watch?v=tCwkiOTlvrs.

[23] Wefers K, Misra C. Oxides and hydroxydes of aluminum. Alcoa Laboratories; 1987. p. 66–8.

[24] Wang HZ, Leung DYC, Leung MKH, Ni M. A review on hydrogen production using aluminum and aluminum alloys. Renewable Sustainable Energy Rev 2009;13:845–53. https://doi.org/10.1016/j.rser.2008.02.009.

[25] Kader MS, Zeng W, Johnston E, Buckner SW, Jelliss PA. A novel method for generating H_2 by activation of the μAl-water system using aluminum nanoparticles. Appl Sci 2022;12(11):5378. https://doi.org/10.3390/app12115378. 2022.

[26] Haller MY, Amstad D, Dudita M, Englert A, Häberle A. Combined heat and power production based on renewable-aluminum-water reaction. Renew Energy 2021;174:879–93. https://doi.org/10.1016/j.renene.2021.04.104.

[27] Gany A, Elitzur S, Rosenband V. J Shipp Ocean Eng 2015;5:151–8. https://doi.org/10.17265/2159-5879/2015.04.001.

[28] Joannopoulos JD, Meade RD, Winn JN. Photonic crystals: molding the flow of light. Princeton: Princeton University Press; 1995.
[29] Yablonovitch E. Photonic band-gap crystals. J Phys Condens Matter 1999;5(16): 2443–60. https://doi.org/10.1088/0953-8984/5/16/004.
[30] Nikitov SA, Tailhades Ph, Tsai CS. Spin waves in periodic magnetic structures: magnonic crystals. J Magn Magn Mater 2001;236:320–30. https://doi.org/10.1016/S0304-8853(01)00470-X.
[31] Gulyaev YV, Nikitov SA, Zhivotovski LV, Klimov AA, Tailhades Ph, Presmanes L, et al. Ferromagnetic films with magnon bandgap periodic structures: magnon crystals. JETP Lett 2003;77(10):567–70. https://doi.org/10.1134/1.1595698.
[32] Kushwaha MS, Halevi P, Dobrzynski L, Djafari-Rouhani B. Acoustic band structure of periodic elastic composites. Phys Rev 1993;71(13):2022–5. https://doi.org/10.1103/PhysRevLett.71.2022.
[33] Rosenband V, Gany A. Application of activated aluminum powder for generation of hydrogen from water. Int J Hydrogen Energy 2010;35:10898–904. https://doi.org/10.1016/j.ijhydene.2010.07.019.
[34] Trunov MA, Schoenitz M, Zhu X, Dreizin EL. Effect of polymorphic phase transformations in Al_2O_3 film on oxidation kinetics of aluminum powders. Combust Flame 2005;140:310–8. https://doi.org/10.1016/j.combustflame.2004.10.010.
[35] Kovarik L, Bowden M, Szanyi J. High temperature transition aluminas in δ-Al_2O_3/θ-Al_2O_3 stability range: review. J Catal 2021;393:357–68. https://doi.org/10.1016/j.jcat.2020.10.009.
[36] Mirhashemihaghighi S, Światowska J, Maurice V, Seyeux A, Zanna S, Salmi E, et al. Corrosion protection of aluminum by ultra-thin atomic layer deposited alumina coatings. Corrosion Sci 2016;106:16–24. https://doi.org/10.1016/j.corsci.2016.01.021.
[37] Wang Q, Liu J, Lei Z, Mou Y, Chen M. Computational and experiments exploration of convection on Cu filling characteristics of multiple aspect-ratio micro through-holes. Electrochim Acta 2022;416:140218. https://doi.org/10.1016/j.electacta.2022.140218.